Title

Multiple origins of extra electron diffractions in fcc metals.

Journal

Science Advances, 10(31)

Authors

Walsh, Flynn
Zhang, Mingwei
Ritchie, Robert
et al.

Publication Date

2024-08-02

DOI

10.1126/sciadv.adn9673

Peer reviewed

MATERIALS SCIENCE

Multiple origins of extra electron diffractions in fcc metals

Flynn Walsh[1]†‡, Mingwei Zhang[1,2,3,4]*†, Robert O. Ritchie[1,3], Mark Asta[1,3], Andrew M. Minor[1,2,3]*

Diffuse intensities in the electron diffraction patterns of concentrated face-centered cubic solid solutions have been widely attributed to chemical short-range order, although this connection has been recently questioned. This article explores the many nonordering origins of commonly reported features using a combination of experimental electron microscopy and multislice diffraction simulations, which suggest that diffuse intensities largely represent thermal and static displacement scattering. A number of observations may reflect additional contributions from planar defects, surface terminations incommensurate with bulk periodicity, or weaker dynamical effects.

INTRODUCTION

High-entropy alloys were originally conceived as crystalline solid solutions with effectively ideal configurational entropies, i.e., complete compositional disorder. Over the past decade, however, it has become increasingly apparent that alloys of multiple principal elements can contain chemical short-range order (SRO) among neighboring atoms (*1*). While there exists little agreement on the nature, extent, or relevance of the ordering realized in most systems, the angstrom-scale chemical structure of concentrated alloys remains intensively investigated as a tantalizing scientific question with potential implications for the unprecedented damage tolerance of materials such as CrCoNi (*2*–*5*).

In the latter half of the last century, SRO in binary alloys was commonly characterized using the diffuse scattering of monochromatic x-rays or neutrons, which can semiquantitatively characterize mean-field chemical environments (*6*), although the interpretation of measurements becomes rapidly more challenging with increasing compositional complexity (*7*). Moreover, these methods require specialized synchrotron experiments and the preparation of single-crystalline samples. Most contemporary characterization efforts have thus preferred to analyze diffraction patterns (DPs) obtained from transmission electron microscopy (TEM), which can spatially resolve local features in two dimensions in a manner that may be complemented by techniques such as strain or composition mapping.

Most of this work has examined face-centered cubic (fcc) alloys containing several 3*d* transition metals as principal elements, which are the subject of this article. While structural specifics may vary among systems, the reduction of unfavorable V-V (*8*, *9*) and Cr-Cr (*7*, *10*) nearest-neighbor pairs is generally expected, as may largely be explained by electrostatic interactions arising from interatomic charge transfer (*11*). The kinetics of this type of ordering are not well established, but recent results suggest that SRO can at least initially form quite rapidly (*12*, *13*), such that a substantial degree may be effectively ubiquitous.

Electron DPs from this class of alloys consistently exhibit intensities that have been widely, though not universally, attributed to SRO. Specific observations, which depend on the crystallographic zone axis (ZA) of incident electrons, are explicitly chronicled in (*14*). As detailed in Materials and Methods, Fig. 1 reproduces the three main features of interest in a representative, water-quenched CrCoNi alloy: streaking in the [110] ZA (Fig. 1A), diffuse $\frac{1}{3}\{422\}$ superlattice intensities in the $[\bar{1}1\bar{1}]$ ZA (Fig. 1B), and diffuse $\frac{1}{2}\{311\}$ superlattice intensities in the $[\bar{1}12]$ ZA (Fig. 1C). As a reference, the diffractions expected from perfect lattices of random CrCoNi are provided in Fig. 1A (D to F), as calculated using multislice simulations that are described in Materials and Methods. Figure 1 (E and F) contains a few very faint "forbidden" diffractions, which are attributed to dynamical scattering that is discussed later.

The diffuse $\frac{1}{2}\{311\}$ intensities in the $[\bar{1}12]$ DP shown in Fig. 1C could, in principle, originate from previously proposed CuPt-type ($L1_1$) ordering, but this form of SRO would also cause missing $\frac{1}{2}\{111\}$ diffractions (*14*), as well as equivalent intensities in other ZAs. CuPt-type ordering is additionally inconsistent with the predictions of standard theoretical methods, as explicitly shown in fig. S1. Further casting doubt on the observation of SRO, Miller (*15*) noted the existence of $\frac{1}{3}\{422\}$ intensities in pure Ni, while Li *et al.* (*16*) more recently reported $\frac{1}{3}\{422\}$ and $\frac{1}{2}\{311\}$ diffractions in pure Cu. Nonetheless, despite some speculation (*14*–*18*), an alternative explanation for these results has heretofore not been established. Here, a combination of TEM techniques and diffraction simulations are used to demonstrate that static and thermal displacements can account for most previously reported observations, with certain results attributable to stacking faults (SFs), surface terminations, and dynamical scattering.

RESULTS

Extra diffractions from thermal displacements

Thermal scattering (*19*, *20*) was, in fact, one of the earliest interpretations of diffuse intensities in concentrated fcc alloys (*17*), though the explanation does not seem concretely established. As detailed in Materials and Methods, diffraction simulations can approximate thermal excitations by displacing atoms from their ideal positions according to experimentally informed normal distributions. Figure 1 (G to I)

[1]Materials Sciences Division, Lawrence Berkeley National Laboratory, Berkeley, CA, USA. [2]National Center for Electron Microscopy, Lawrence Berkeley National Laboratory, Berkeley, CA, USA. [3]Department of Materials Science and Engineering, University of California, Berkeley, Berkeley, CA, USA. [4]Department of Materials Science and Engineering, University of California, Davis, Davis, CA, USA.
*Corresponding author. Email: mwwzhang@ucdavis.edu (M.Z.); aminor@berkeley.edu (A.M.M.)
†These authors contributed equally to this work.
‡Present address: Lawrence Livermore National Laboratory, Livermore, CA, USA.

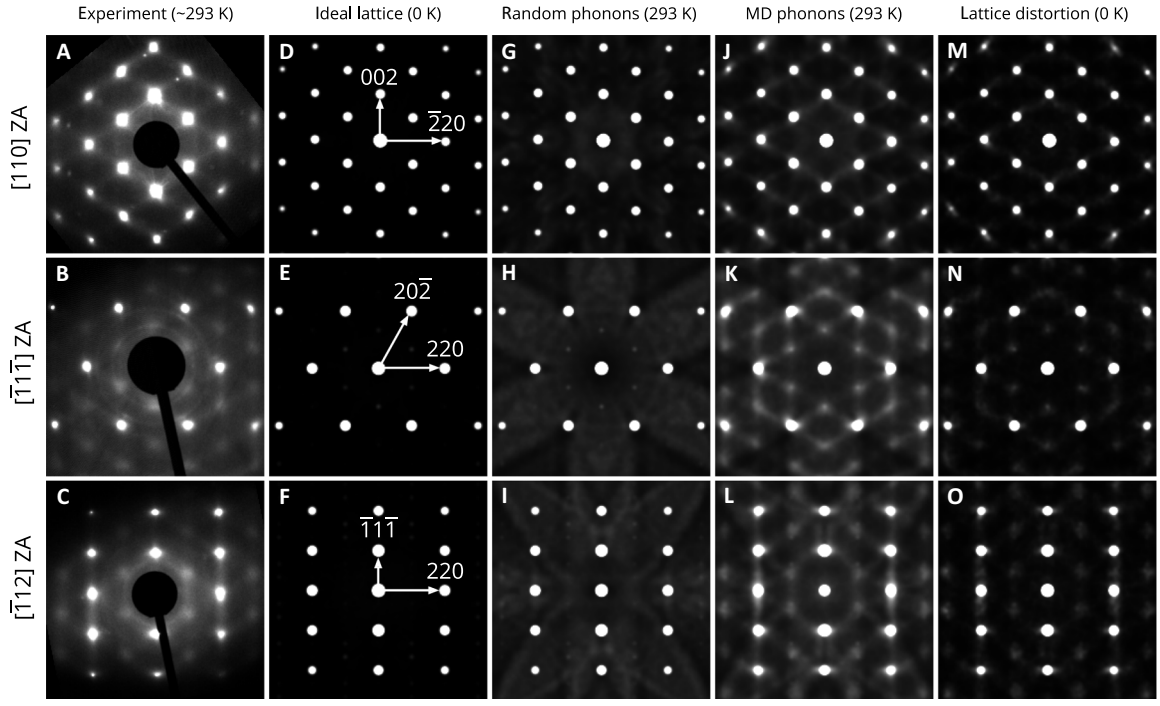

Fig. 1. Extra diffractions from thermal and static displacement scattering in CrCoNi. Selected-area electron DPs of CrCoNi containing (**A**) streaking in the [110] ZA, (**B**) diffuse $\frac{1}{3}\{422\}$ intensities in the [$\bar{1}1\bar{1}$] ZA, and (**C**) diffuse $\frac{1}{2}\{311\}$ intensities in the [$\bar{1}12$] ZA. Coordinates are given in (**D**) to (**F**), which provide equivalent DPs calculated for ideal lattices of disordered CrCoNi. (**G** to **I**) Diffuse scattering expected from random thermal displacements. (**J** to **L**) Calculations for more realistic MD trajectories, which largely reproduce experiment in the [$\bar{1}1\bar{1}$] and [$\bar{1}12$] ZAs. (**M**) to (**O**) consider static displacement scattering from lattice distortion, which causes weaker versions of the same intensities.

shows that random deviations from perfect lattice sites cause relatively uniform diffuse scattering but cannot account for specific extra diffractions. More realistically, Fig. 1 (J to L) presents DPs calculated for snapshots of molecular dynamics (MD) simulations driven by a "machine learning" interatomic potential (*12*), which are further described in Materials and Methods. Some faint streaking appears in the [110] DP in Fig. 1J, though this seems somewhat weaker than in, for example, (*21*). More clearly, calculations for the [$\bar{1}1\bar{1}$] Fig. 1K and [$\bar{1}12$] (Fig. 1L) ZAs predict DPs that closely resemble the experiments shown in Fig. 1 (B and C). All simulations considered chemically random structures, but fig. S6 offers equivalent predictions for configurations containing an approximate model of ordering. That is, SRO appears to negligibly affect ambient-temperature DPs.

Considering broad similarities in the phonon spectra of fcc metals (*22*), the same phenomenon is expected to explain observations in other systems. Figure S7 predicts comparable thermal scattering in pure Cu, reproducing the DPs reported in (*16*). Experimentally, thermal scattering can be isolated by considering, in addition to DPs, the Fourier transforms (FTs) of atomic-resolution scanning transmission electron microscopy (STEM) images. As directly imaged atomic positions represent time averages, specific intensities from thermal scattering should disappear (*19*). Accordingly, extra diffractions in, for example, the FTs of VCoNi images (*9*) must have originated through other means. Diffuse $\frac{1}{3}\{422\}$ intensities in the 77-K DP of a Ni-Cr–based alloy (*15*) could also have a distinct source, though fig. S7 suggests that thermal scattering may not be negligible at this temperature.

Extra diffractions from static displacements

Possibly explaining these observations, Fig. 1 (N and O) demonstrates that the introduction of energetically favorable lattice distortion through structural relaxation (see Materials and Methods) produces weaker versions of the diffuse intensities seen in Fig. 1 (K and L). This static displacement scattering has been studied historically (*6*, *19*, *23*) and was previously proposed as a potential source of extra diffractions in concentrated fcc alloys (*18*, *24*). Equivalent $CrNi_2$ configurations, which are representative of the alloy considered in (*15*), cause similar displacement scattering, but extra diffractions are largely absent from calculations for $CoNi_2$, which forms a more ideal lattice on account of the chemical similarity of the two elements (*25*). V, which electronegatively resembles Cr, is expected to cause comparable or greater scattering in VCoNi. Simulations presented in fig. S6 suggest that SRO may somewhat reduce displacement scattering relative to random alloys, though it is not clear whether this effect would be practically detectable.

Applying random displacements to relaxed structures primarily adds background intensity, confirming that correlated thermal displacements contribute a distinct, stronger effect, rather than amplify 0-K relaxations. Together, static and thermal displacement scattering can explain every measurement of which we are aware, except the FT of a high-angle annular dark-field (HAADF) STEM image of [111]-oriented Cu (*16*), where the innermost $\frac{1}{3}\{422\}$ diffractions appear as sharp peaks. (Similar analysis was not provided for the [112] ZA.)

Extra diffractions from dynamical amplification

It is not impossible that the extra diffractions in the FT of Cu (*16*) originated from hidden planar defects, which would be accommodated by the low SF energy of Cu and are examined in more detail later. However, the faint intensities in Fig. 1E indicate that the same extra diffractions can, in principle, occur in perfect lattices. The nature of these features is inferred from calculations for varying-thickness Ni foils presented in Fig. 2. Experimental DPs from a ~120-nm thick sample in the $[\bar{1}1\bar{1}]$ (Fig. 2A) and $[\bar{1}12]$ (Fig. 2B) ZAs are provided for reference. Thermal scattering, which is weaker in Ni than Cu (*26*) or CrCoNi (*27*), is not readily visible in Fig. 2B, though likely contributed to the extra diffractions in Fig. 2A. Still, these results provide a benchmark for theoretical calculations, which considered only random thermal excitations to isolate scattering from other sources.

Figure 2C predicts that non-negligible $\frac{1}{3}\{422\}$ diffractions will always appear in the $[\bar{1}1\bar{1}]$ ZA of ~15 to 100 nm foils. The absence of strong intensities below ~15 nm suggests that they arise through multiple scattering events that increase in frequency with sample thickness, though this phenomenon is generally understood to modify existing intensities, not generate new diffractions (*19*). Absent other sources, these features could ultimately originate from otherwise negligible higher-order Laue zone (HOLZ) diffraction, that is, scattering between, rather than within, reciprocal lattice planes normal to the ZA, as was suggested in (*15*). Specifically, in the $[\bar{1}1\bar{1}]$ ZA, kinematically miniscule $(11\bar{1})$ diffractions from the immediately above plane of the reciprocal lattice would be projected onto $\frac{1}{3}(42\bar{2})$, while $(1\bar{1}1)$ projections from the plane below would appear as $\frac{1}{3}(2\bar{2}4)$, etc. Reduced intensities above ~100 nm would be consistent with the decay of underlying HOLZ diffractions with increasing sample thickness. While this dynamical scattering explains the faint peaks in Fig. 1 (E, F, H, and I), it is not expected to majorly contribute to the DP of the 120-nm foil displayed in Fig. 2A.

Figure 2D provides equivalent calculations for the $[\bar{1}12]$ ZA, where (111) diffractions in the above plane of the reciprocal lattice could be projected to $\frac{1}{3}(421)$, while $(11\bar{1})$ in the plane below could appear at $\frac{1}{3}(24\bar{1})$, etc. These locations are marked in Fig. 2B, though no such scattering is visible experimentally, consistent with the comparably minimal intensities predicted in Fig. 2D.

Extra diffractions from surface terminations

As discussed in Materials and Methods, all structures simulated up to this point have been periodic. However, a complete investigation must account for samples in which the number of atomic layers along the ZA is not a multiple of the bulk periodicity. For example, a [111]-oriented foil can consist of $3m$ commensurate layers, where m is an integer, or $3m \pm 1$ incommensurate layers, which are known to produce $\frac{1}{3}\{422\}$ intensities, plus reciprocal lattice translations. Similarly, there exist six possible planar terminations of [112] and two of [110]. As more recently noted in (*15*, *16*), the study in (*28*) demonstrated this phenomenon in Au films deposited in (111) layers, for which dark-field (DF) images reveal surface contours corresponding to atomic steps.

In conventional jet-polished TEM samples, DF apertures around diffuse intensities highlight nanometer-scale features that have been previously interpreted as ordered domains. Following (*28*), these could instead correspond to tiny surface islands of varying atomic thickness, in which case standard DPs sampling hundreds of nm^2 would simultaneously represent many different commensurate and incommensurate stacking terminations.

Calculations for all types of surface termination are individually presented in fig. S8 and averaged in Fig. 2 for the $[\bar{1}1\bar{1}]$ (Fig. 2E) and $[\bar{1}12]$ (Fig. 2F) ZAs, analogous to commensurate calculations in Fig. 2 (C and D). Incommensurate surface terminations generate the same extra diffractions, though with much greater intensity. Calculations for the $[\bar{1}1\bar{1}]$ ZA in Fig. 2B predict $\frac{1}{3}\{422\}$ diffractions of magnitude

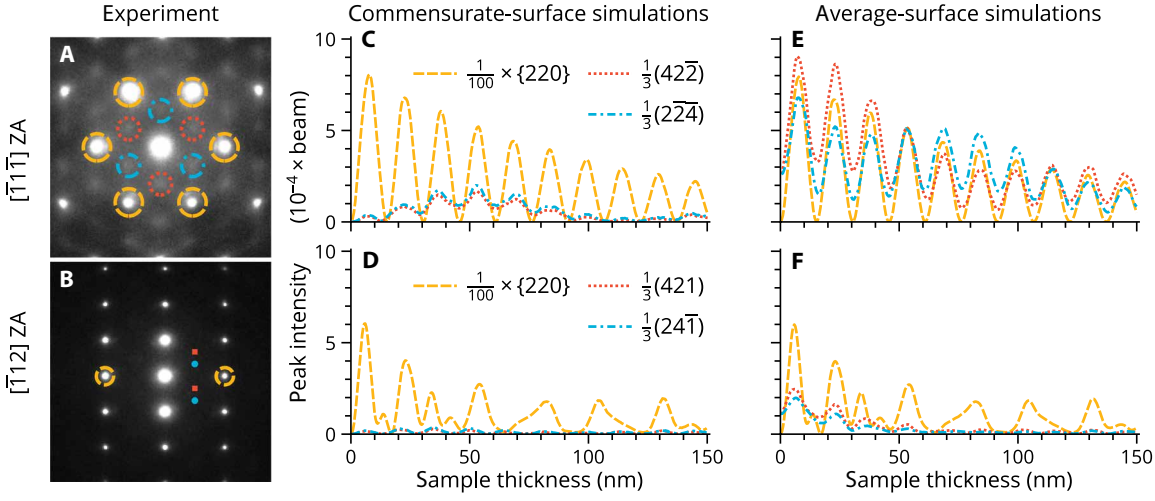

Fig. 2. Extra diffractions from dynamical scattering and incommensurate surface terminations in Ni. Experimental DPs from a ~120 nm Ni foil in the (**A**) $[\bar{1}1\bar{1}]$ and (**B**) $[\bar{1}12]$ ZAs. Annotations indicate {220} lattice diffractions (yellow dashes) and locations where two sets of extra diffractions can theoretically occur (red dots and blue dot-dashes). See Fig. 1 for coordinates. (**C** and **D**) Peak intensities at the highlighted locations in simulations of periodic Ni configurations with random thermal displacements. Reference {220} intensities are plotted at $^1/_{100}$ scale. Clear extra diffractions are predicted in (C), if not (D). (**E**) and (**F**) are equivalent to (C) and (D) for simulations considering all possible surface terminations. Each datum represents an average of (E) three or (F) six possible stacking multiples, which are predicted to cause the same extra diffractions that occur in commensurate configurations.

not incomparable to experimental values shown in Fig. 2A. While the simulated features are sharper than in ambient temperature experiments, which presumably include thermal scattering, the demonstrated athermal effect could contribute to low-temperature and real-space observations. Intriguingly, calculations suggest that the diffuse intensities could split into two groups corresponding to $\frac{1}{3}(42\bar{2})$ and $\frac{1}{3}(22\bar{4})$, plus reciprocal lattice translations—this has not, to our knowledge, been observed experimentally. The extra diffraction predicted for the $[\bar{1}12]$ ZA in Fig. 2F remain small, though calculations indicate that intensities could be more detectable in very thin samples. As shown in fig. S8, this mechanism does not explain observations in the [110] ZA.

Extra diffractions from planar defects

While previously considered phenomena can fully account for results in the [111] and [112] ZAs, it is worth noting that all the features of interest can also be caused by SFs, which are usually readily visible in TEM, particularly when using bright-field or DF imaging modes with diffraction contrast. Conventional microscale faulting can explain recently reported "mechanically-driven SRO" (*29*), where extra diffractions likely originated from SFs formed between Shockley partials dissociated across slip bands induced by mechanical deformation. The creation of Frank loops, which enclose SFs, by ion irradiation (*30*) can similarly account for recently proposed "irradiation-assisted SRO" (*31*). Besides these apparent SFs caused by mechanical deformation or ion irradiation, conventional sample preparation methods, namely, Ar ion milling and Ga focused ion beam (FIB) milling, can inadvertently introduce Frank loops with diameters as small as 2 to 5 nm on foil surfaces, as shown in fig. S3 (G and H). This type of defect could affect results in ion-milled samples (*4*, *32*), but most TEM specimens, including those examined in this study, are instead prepared only by electropolishing, which does not introduce structural imperfections.

We have previously speculated (*14*) that less obvious nanoscale SF tetrahedra (SFTs) or Frank loops could nonetheless form during bulk sample processing. Consistent with this hypothesis, figs. S4 and S5 reveal a remarkable abundance of previously unreported SFTs in water-quenched CrCoNi. However, streaking in the [110] ZA is not widespread, while $\frac{1}{2}\{311\}$ diffractions are equally present in slow-cooled samples, which do not contain quench-induced faulting. The absence of planar defects in slow-cooled samples is demonstrated in Fig. 3, which presents DF (Fig. 3, A and F) and high-resolution STEM (HRSTEM) (Fig. 3, D and I) images for the [110] and $[\bar{1}12]$ ZAs of the same region. While nanoscale faulting can locally cause streaking, Fig. 3 (B and C) shows that the feature is often absent from larger-scale DPs. In contrast, Fig. 3 (G and H) indicates that a $\frac{1}{2}\{311\}$ superlattice persists independent of processing conditions. Defects smaller than 2 nm could theoretically escape detection by HR(S)TEM, but such features would not be expected to contribute to typical DPs. It remains possible that specific observations of streaking in the [110] ZA reflect larger, more heterogeneously distributed planar defects.

DISCUSSION

Building on (*15*), Coury *et al.* (*33*) very recently proposed that the HOLZ diffraction examined in Fig. 2 (C and D) is the common source of widely observed diffuse intensities. However, it is not clear if the phenomenon can be generally distinguished from theoretically stronger surface contributions examined in Fig. 2 (E and F). Of course, these effects are greatly complicated by the true conditions of foil surfaces, which, for the considered alloys, inevitably host nanometer-scale oxides. Analysis is further obfuscated by the reality that TEM ZAs rarely correspond to actual surface normals with associated steps but are instead obtained by tilting grains with arbitrary surface planes. Even though the effect of surface steps might be more muted under realistic experimental conditions, we do not believe that they can altogether be dismissed.

In any case, dynamically amplified HOLZ diffraction seems less relevant outside of the [111] ZA. Contrary to prior assertions (*15*),

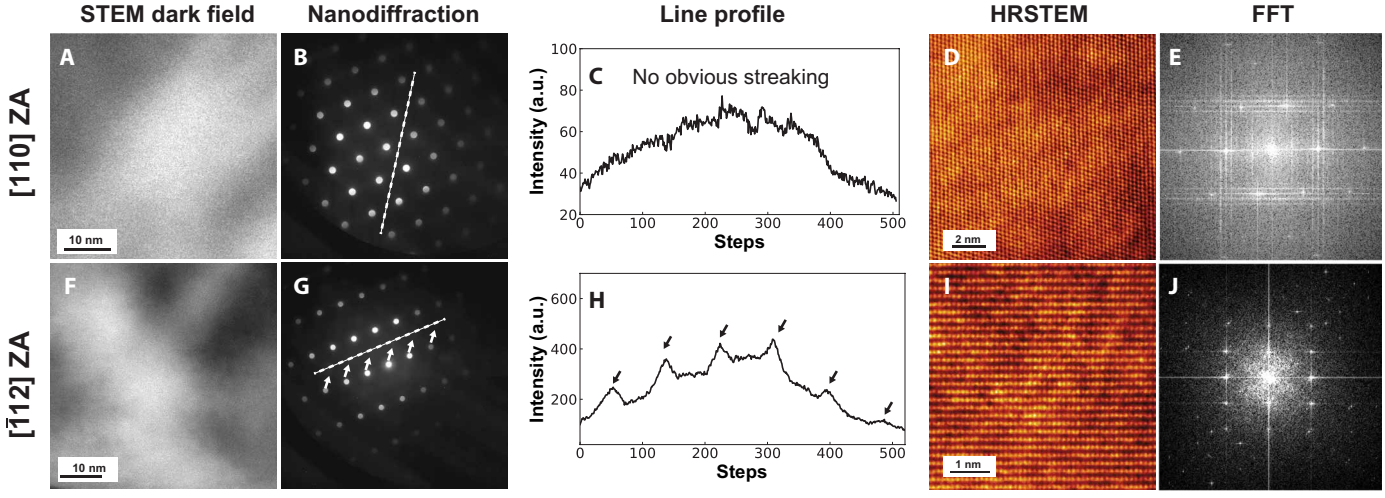

Fig. 3. Absence of planar defects in slow-cooled CrCoNi samples. (**A**) STEM-DF image of a 20 to 30 nm-thick region (down-to-up) in a slow-cooled CrCoNi sample along the [110] ZA; (**B**) summed nanoDP from (A); (**C**) the intensity profile of the dashed line marked in (B), showing no obvious streaking; (**D**) atomic-resolution STEM–low-angle annular DF image showing no SFTs; (**E**) the FT of (D), showing no streaking along ⟨111⟩ g-vectors; and (**F** to **J**) equivalent to (A) to (E) for the same region in the $[\bar{1}12]$ ZA. Despite the absence of defects, the line profile given in (H) shows clear diffuse $\frac{1}{2}\{311\}$ superlattice peaks, as indicated by the black arrows.

this mechanism does not produce experimentally observed $\frac{1}{2}\{311\}$ intensities in the [112] ZA, rather tiny peaks at positions such as $\frac{1}{3}(421)$, which are identified in Fig. 2B. The study in (*33*) provides nominally correct projections in the [112] ZA, but these are not plotted in exactly the right positions—sharp HOLZ diffractions lie outside, not within, many observed features. It is thus unclear how adjacent $\frac{1}{3}\{421\}$ diffractions could generate $\frac{1}{2}\{311\}$ intensities, though they could be subsumed into diffuse scattering from other sources, which occurs to an extent in Fig. 1 (L and O). Still, the proximity of displacive and HOLZ intensities is not necessarily coincidental, as local lattice distortions and thermal excitations could, in principle, generate intensities via out-of-plane scattering. Detailed analysis of possible connections is beyond the scope of this study, which aims to practically explain observations in the literature.

As a final note, it is worth emphasizing the extent to which both lattice and diffuse intensities vary with sample thickness, as seen in Fig. 2. This effect should be less extreme in real experiments, in which electrons are not ideally monochromatic and samples vary in height, but thickness differences can still compromise comparison between any two specimens. For example, the absence of clear diffuse intensities in one observation of an unaged alloy implies relatively little about the origin of intensities in an aged alloy, particularly when lattice diffractions in the unaged DP are also considerably weaker (*34*). This is to say nothing of local variations in surface topography and oxides. Differences in intensities reported in our earlier work (*35*) could similarly be explained by variations in sample details.

To summarize, diffuse intensities previously attributed to SRO are caused by a number of phenomena generally associated with the breaking of lattice symmetry. The greatest source of this scattering appears to be correlated, though not random, thermal displacements, which likely contributed to most reciprocal-space observations in the [111] and [112] ZAs. Intensities in FTs and low-temperature DPs of concentrated alloys could instead represent static displacement scattering, which qualitatively produces the same features. Extra diffractions in the [111] ZA can also be caused by incommensurate surface terminations, though further work is needed to understand these effects in realistic samples. Dynamical artifacts also appear at the same locations but to a lesser extent that seems insufficient to explain most observations.

In some studies, extra diffractions may primarily reflect planar defects, though in most cases, these were otherwise apparent. While an unexpected abundance of nearly invisible SFTs was found in quenched CrCoNi, these appear not to affect larger-scale DPs and were not observed in slow-cooled samples. There is relatively little evidence that measured diffuse intensities directly relate to SRO, which may still widely exist in concentrated 3*d* alloys.

MATERIALS AND METHODS

Specimen processing

Equiatomic CrCoNi alloys were produced by arc-melting high-purity (>99.9%) elements under an Ar atmosphere followed by drop casting into 127 × 19.1 × 25.4-mm Cu molds. As-cast samples were homogenized in vacuum at 1200°C for 24 hours and cold-rolled to a final thickness of 6.1 mm (76% reduction). Samples were then recrystallized at 1000°C for 0.5 hours, followed by either ice water quenching or slow furnace cooling.

Transmission electron microscopy

Energy-filtered selected-area electron DPs were obtained on a Zeiss monochromated LIBRA 200MC microscope at an accelerating voltage of 200 kV in the [110], $[\bar{1}1\bar{1}]$, and $[\bar{1}12]$ ZAs. Inelastically scattered electrons were filtered by an in-column Ω energy filter using an energy slit of 5 eV. While thermal scattering is technically inelastic, electron energies are only minimally affected by interactions with phonons (*19*), which typically have energies below 1 eV, so thermal scattering should not be removed by standard filters.

STEM imaging of quenched and slow-cooled CrCoNi was performed on the Transmission Electron Aberration-corrected Microscope I at the National Center for Electron Microscopy at Lawrence Berkeley National Laboratory. A wide range of microscope parameters in terms of C2 aperture sizes, convergence angles (α), current densities, and camera lengths (CLs) were explored to acquire optimal images for each imaging technique. Diffraction-contrast bright- and dark-field STEM imaging was carried out under $\vec{g} = 200$ two-beam conditions near the [110] ZA using a 5-μm C2, an α of 1.1 mrad, and CLs from 2.2 to 4.3 m. Scanning nanobeam diffraction, or four-dimensional STEM (4DSTEM) was performed using a 5 or 10-μm C2 and resulting α of 1.1 or 2.3 mrad and probe sizes of 1 and 0.7 nm, and CLs from 0.63 to 0.8 m in [110] and $[\bar{1}12]$ ZA on a Gatan K3 camera. Because a trade-off exists between real space and reciprocal space resolution, the convergence angle was selected between these two values based on an ad hoc basis. Inelastically scattered electrons were filtered by a postcolumn Gatan Imaging Filter Continuum K3 spectrometer using an energy slit of 20 eV. Raw 4DSTEM data were processed by the py4DSTEM package (*36*). HRSTEM was conducted in the same locations as in 4DSTEM scans using a 70-μm C2 and an α of 16 mrad. A large CL of 0.8 m was used to ensure the images were taken under low-angle annular DF to capture the diffraction contrast originating from crystal defects. Conventional HAADF was not used because CrCoNi provides very limited Z-contrast. The probe was corrected using a CEOS DCOR spherical-aberration corrector to an outer tableau tilt of 35 mrad and C1, A1, A2, B2, C3, A3, S3, C5 values of −2.5 nm, 2.4 nm, 15.5 nm, 20.0 nm, 103.8 nm, 96.8 nm, 104.4 nm, and −771 μm, respectively.

TEM samples were prepared by the following steps: mechanical polishing to a final thickness of 50 μm using 320/600/800/1200 grit papers; punching out 3-mm discs from the foils and dimpling on one side to a center thickness of ~20 μm, and eventually achieving perforation by twin-jet polishing on a Fischione Model 110 electropolisher in an electrolyte of 70% methanol, 20% glycerol, and 10% perchloric acid at −30°C under a stable current of ~25 mA. Care has been taken to ensure that the thinnest part of the jet-polished samples was 20 to 30 nm, which was confirmed by the electron energy-loss spectroscopy log-ratio technique.

To examine possible artifacts caused by argon ion milling, selected jet-polished samples were further ion-milled by a Gatan PIPS II precision ion-polishing system under a voltage of 3 kV for 1 hour, followed by 1 kV for 15 min and 0.5 kV for 30 min. The guns were aligned to ±3°. Alternatively, FIB-liftout samples were prepared on an FEI Scios 2 DualBeam FIB/SEM under an operating voltage of 30 kV followed by polishing at 5 and 2 kV. The FIB lamellae were then polished on a Fischione Model 1040 Nanomill under voltages of 900 and 500 V for 20 min to further alleviate FIB damage. The ion-milled and FIB-milled. samples also have a final thickness of 20 to 30 nm. These samples were characterized by an FEI F20 UT Tecnai STEM under an accelerating voltage of 200 kV.

Diffraction simulations

Multislice diffraction simulations were performed using abTEM (*37*) with atomic scattering potentials parameterized as in (*38*). For the calculations displayed in Fig. 1, potentials were projected onto 0.25-Å slices using finite integrals and a sampling resolution of 0.02 $Å^{-1}$. All simulation cells were 10 nm by 10 nm in directions normal to the ZA, with varying thicknesses. CrCoNi configurations were ~27.5-nm thick, with the goal of representing ~20 to 30 nm samples experimentally considered in this study and the 30-nm samples considered in (*9*). Structures for the [110], $[\bar{1}1\bar{1}]$, and $[\bar{1}12]$ ZAs respectively contained 218, 135, and 378 atomic layers along the ZA. While a comprehensive thickness study with realistic displacements is hardly feasible, this height seems to represent average scattering conditions in the vicinity, with stronger dynamical effects calculated for ~25-nm configurations and weaker effects calculated for ~30-nm configurations, consistent with the findings displayed in Fig. 2. These simulations are intended to qualitatively demonstrate the discussed scattering mechanisms, not as explicitly quantitative predictions.

Because of the large number of simulations involved, calculations for Fig. 2 used a slightly more approximate 0.5-Å slice thickness, 0.05-$Å^{-1}$ sampling, and infinite integral projections. The difference in parameters was found to only minimally affect calculations for finite-temperature configurations, though in some cases even larger pixel sizes were noted to exaggerate extra diffractions. All calculated DPs are linearly plotted over the intensity range 0 to 1.2×10^{-5}, where the original beam intensity is 1, using the matplotlib (*39*) colorscheme "binary_r." Experimental DPs are plotted similarly, albeit without definitive intensity normalization. As the assumption of ideally monochromatic plane waves in multislice simulations produces unrealistically sharp DPs, a Gaussian filter with a width of 2 pixels was applied to all plotted images, which slightly diffuses, though in sum preserves, calculated intensities. These consistent settings were chosen to approximately reproduce the lattice diffractions in comparable experiments, while also clearly showing various diffuse intensities. It should be noted that this procedure somewhat reduces the visibility of dynamical artifacts, which are typically single pixels, but this effect is expected to be realistic and may explain why intensities such as $\frac{1}{3}\{421\}$ are not seen in experiments. All quantitatively reported intensities represent local maxima before filtering.

Random phonons were modeled using 16 configurations with normally distributed displacements with experimentally informed SDs of 0.06714 Å for Ni (*26*) and 0.0922 Å for CrCoNi (*27*). The equivalent value for Cu, which was not used, is 0.08935 Å (*26*).

Molecular statics and dynamics

Static structural relaxations and MD simulations were performed using LAMMPS (*40*). To model 0 K lattice distortion, atomic positions were energetically optimized following a conjugate-gradient algorithm until the collective norm of all forces was below 10^{-12} eV/Å. Realistic phonons were obtained by averaging 16 MD snapshots, which were taken every 2000 steps after 10,000 steps of equilibration, where each step is 1 fs under a standard Nosé-Hoover thermostat.

For computational simplicity, simulations used fixed lattice parameters according to experimental values at ambient conditions, that is 3.524 Å for Ni, 3.615 Å for Cu (*41*), and 3.56 Å for CrCoNi (*42*). Constant-pressure simulations were found to produce equivalent DPs. CrCoNi was modeled using the neural network potential (*43*) described in (*12*). It should be noted that while this model seems to reasonably represent underlying density-functional theory calculations, a widely used embedded-atom method potential (*44*), which does not realistically describe atomic interactions (*10*), predicts structures without notable static displacement scattering. To isolate the effects of dynamical scattering and surface terminations, which would be confounded by thermal scattering in the same locations, Ni was modeled only as an ideal lattice with random thermal displacements.

Both periodic and free surfaces in the direction of the ZA were considered. While the latter may seem more realistic, the CrCoNi potential displayed some instabilities in the presence of free surfaces. In addition, MD simulations of surfaces exhibited unphysically large swaying motions that were likely related to the lack of constraint and imposition of periodic boundary conditions perpendicular to the ZA. These could be eliminated through careful optimization of the thermostat, but DPs were otherwise identical to fully periodic calculations, which were used instead for convenience.

Supplementary Materials

This PDF file includes:

Figs. S1 to S8
References

REFERENCES AND NOTES

1. F. Walsh, A. Abu-Odeh, M. Asta, Reconsidering short-range order in complex concentrated alloys. *MRS Bull.* **48**, 753–761 (2023).
2. D. Liu, Q. Yu, S. Kabra, M. Jiang, P. Forna-Kreutzer, R. Zhang, M. Payne, F. Walsh, B. Gludovatz, M. Asta, A. M. Minor, E. P. George, R. O. Ritchie, Exceptional fracture toughness of CrCoNi-based medium- and high-entropy alloys at 20 kelvin. *Science* **378**, 978–983 (2022).
3. P. Yu, J.-P. Du, S. Shinzato, F.-S. Meng, S. Ogata, Theory of history-dependent multi-layer generalized stacking fault energy–A modeling of the micro-substructure evolution kinetics in chemically ordered medium-entropy alloys. *Acta Mater.* **224**, 117504 (2022).
4. S. Picak, P. Singh, D. Salas, M. A. Tunes, X. Fang, L. Zhou, M. J. Kramer, Y. I. Chumlyakov, D. D. Johnson, R. Arroyave, Y. Ren, I. Karaman, Orientation dependence of the effect of short-range ordering on the plastic deformation of a medium entropy alloy. *Mater. Sci. Eng. A* **888**, 145309 (2023).
5. I. V. Kireeva, Y. I. Chumlyakov, A. A. Saraeva, A. V. Vyrodova, Physical factors controlling large shape memory effect in FCC ↔ HCP martensitic transformation in crmnfeconi high-entropy-alloy single crystals. *Metals* **13**, 1755 (2023).
6. G. E. Ice, C. J. Sparks, Modern resonant x-ray studies of alloys: Local order and displacements. *Annu. Rev. Mater. Sci.* **29**, 25–52 (1999).
7. B. Schönfeld, C. R. Sax, J. Zemp, M. Engelke, P. Boesecke, T. Kresse, T. Boll, T. Al-Kassab, O. E. Peil, A. V. Ruban, Local order in Cr-Fe-Co-Ni: Experiment and electronic structure calculations. *Phys. Rev. B* **99**, 014206 (2019).
8. T. Kostiuchenko, F. Körmann, J. Neugebauer, A. Shapeev, Impact of lattice relaxations on phase transitions in a high-entropy alloy studied by machine-learning potentials. *npj Comput. Mater.* **5**, 55 (2019).
9. X. Chen, Q. Wang, Z. Cheng, M. Zhu, H. Zhou, P. Jiang, L. Zhou, Q. Xue, F. Yuan, J. Zhu, X. Wu, E. Ma, Direct observation of chemical short-range order in a medium-entropy alloy. *Nature* **592**, 712–716 (2021).
10. S. Ghosh, V. Sotskov, A. V. Shapeev, J. Neugebauer, F. Körmann, Short-range order and phase stability of CrCoNi explored with machine learning potentials. *Phys. Rev. Mater.* **6**, 113804 (2022).
11. P. Papež, M. Zelená, M. Friák, I. Dlouhá, The effect of spin-polarization, atomic ordering and charge transfer on the stability of CoCrNi medium entropy alloy. *Mater. Chem. Phys.* **304**, 127783 (2023).
12. J.-P. Du, P. Yu, S. Shinzato, F.-S. Meng, Y. Sato, Y. Li, Y. Fan, S. Ogata, Chemical domain structure and its formation kinetics in CrCoNi medium-entropy alloy. *Acta Mater.* **240**, 118314 (2022).
13. T. Teramoto, K. Kitasumi, R. Shimohara, Y. Ito, R. Shimizu, K. Tanaka, R. Ueji, Formation condition and effect on the early stages of plastic deformation of chemical short-range order in Cr-Co-Ni medium-entropy alloy. *J. Alloys Compd.* **941**, 169016 (2023).
14. F. Walsh, M. Zhang, R. O. Ritchie, A. M. Minor, M. Asta, Extra electron reflections in concentrated alloys do not necessitate short-range order. *Nat. Mater.* **22**, 926–929 (2023).
15. C. Miller, thesis, Colorado School of Mines (2016).

16. L. Li, Z. Chen, S. Kuroiwa, M. Ito, K. Yuge, K. Kishida, H. Tanimoto, Y. Yu, H. Inui, E. P. George, Evolution of short-range order and its effects on the plastic deformation behavior of single crystals of the equiatomic Cr-Co-Ni medium-entropy alloy. *Acta Mater.* **243**, 118537 (2023).
17. X. D. Xu, P. Liu, S. Guo, A. Hirata, T. Fujita, T. G. Nieh, C. T. Liu, M. W. Chen, Nanoscale phase separation in a fcc-based CoCrCuFeNiAl$_{0.5}$ high-entropy alloy. *Acta Mater.* **84**, 145–152 (2015).
18. M. Kawamura, M. Asakura, N. L. Okamoto, K. Kishida, H. Inui, E. P. George, Plastic deformation of single crystals of the equiatomic Cr–Mn–Fe–Co–Ni high-entropy alloy in tension and compression from 10 K to 1273 K. *Acta Mater.* **203**, 116454 (2021).
19. G. Van Tendeloo, S. Amelinckx, The origin of diffuse intensity in electron diffraction patterns. *Phase Transit.* **67**, 101–135 (1998).
20. Z. L. Wang, Thermal diffuse scattering in sub-angstrom quantitative electron microscopy–phenomenon, effects and approaches. *Micron* **34**, 141–155 (2003).
21. R. Zhang, S. Zhao, J. Ding, Y. Chong, T. Jia, C. Ophus, M. Asta, R. O. Ritchie, A. M. Minor, Short-range order and its impact on the CrCoNi medium-entropy alloy. *Nature* **581**, 283–287 (2020).
22. V. N. Antonov, V. Y. Milman, V. V. Nemoshkalenko, A. V. Zhalko-Titarenko, Lattice dynamics of FCC transition metals: A pseudopotential approach. *Z. Phys. B Condens. Matter* **79**, 223–232 (1990).
23. H. E. Cook, The influence of static atomic displacements on the diffuse intensity scattered by solid solutions. *J. Phys. Chem. Solid* **30**, 1097–1112 (1969).
24. D. Zhou, Z. Chen, K. Ehara, K. Nitsu, K. Tanaka, H. Inui, Effects of annealing on hardness, yield strength and dislocation structure in single crystals of the equiatomic Cr-Mn-Fe-Co-Ni high entropy alloy. *Scripta Mater.* **191**, 173–178 (2021).
25. H. S. Oh, K. Odbadrakh, Y. Ikeda, S. Mu, F. Körmann, C.-J. Sun, H. S. Ahn, K. N. Yoon, D. Ma, C. C. Tasan, T. Egami, E. S. Park, Element-resolved local lattice distortion in complex concentrated alloys: An observable signature of electronic effects. *Acta Mater.* **216**, 117135 (2021).
26. L.-M. Peng, G. Ren, S. L. Dudarev, M. J. Whelan, Debye-Waller factors and absorptive scattering factors of elemental crystals. *Acta Crystallogr. A* **52**, 456–470 (1996).
27. F. X. Zhang, S. Zhao, K. Jin, H. Xue, G. Velisa, H. Bei, R. Huang, J. Y. P. Ko, D. C. Pagan, J. C. Neuefeind, W. J. Weber, Y. Zhang, Local structure and short-range order in a NiCoCr solid solution alloy. *Phys. Rev. Lett.* **118**, 205501 (2017).
28. D. Cherns, Direct resolution of surface atomic steps by transmission electron microscopy. *Phil. Mag.* **30**, 549–556 (1974).
29. J. B. Seol, W.-S. Ko, S. S. Sohn, M. Y. Na, H. J. Chang, Y.-U. Heo, J. G. Kim, H. Sung, Z. Li, E. Pereloma, H. S. Kim, Mechanically derived short-range order and its impact on the multi-principal-element alloys. *Nat. Commun.* **13**, 6766 (2022).
30. D. Hull, D. J. Bacon, *Introduction to Dislocations* (Butterworth-Heinemann, ed. 5, 2011).
31. Z. Su, T. Shi, H. Shen, L. Jiang, L. Wu, M. Song, Z. Li, S. Wang, C. Lu, Radiation-assisted chemical short-range order formation in high-entropy alloys. *Scripta Mater.* **212**, 114547 (2022).
32. G. Tang, Z. Zhang, Y. Liu, Y. Wang, X. Wu, X. Liu, Quantifying chemical fluctuations around medium-range orders and its impact on dislocation interactions in equiatomic CrCoNi medium entropy alloy. *Mater. Des.* **225**, 111572 (2023).
33. F. G. Coury, C. Miller, R. Field, M. Kaufman, On the origin of diffuse intensities in fcc electron diffraction patterns. *Nature* **622**, 742–747 (2023).
34. N. Liu, X. Tian, Q. Liu, B. Gan, J. Ding, E. Ma, Z. Wang, Aging elevates chemical short-range order and twinning stress in a CrCoNi medium-entropy alloy. *Sci. China Mater.* **66**, 4220–4225 (2023).
35. M. Zhang, Q. Yu, C. Frey, F. Walsh, M. I. Payne, P. Kumar, D. Liu, T. M. Pollock, M. D. Asta, R. O. Ritchie, A. M. Minor, Determination of peak ordering in the CrCoNi medium-entropy alloy via nanoindentation. *Acta Mater.* **241**, 118380 (2022).
36. B. H. Savitzky, S. E. Zeltmann, L. A. Hughes, H. G. Brown, S. Zhao, P. M. Pelz, T. C. Pekin, E. S. Barnard, J. Donohue, L. Rangel DaCosta, E. Kennedy, Y. Xie, M. T. Janish, M. M. Schneider, P. Herring, C. Gopal, A. Anapolsky, R. Dhall, K. C. Bustillo, P. Ercius, M. C. Scott, J. Ciston, A. M. Minor, C. Ophus, py4DSTEM: A software package for four-dimensional scanning transmission electron microscopy data analysis. *Microsc. Microanal.* **27**, 712–743 (2021).
37. J. Madsen, T. Susi, The abTEM code: Transmission electron microscopy from first principles. *Open Res. Eur.* **1**, 24 (2021).
38. I. Lobato, D. Van Dyck, An accurate parameterization for scattering factors, electron densities and electrostatic potentials for neutral atoms that obey all physical constraints. *Acta Crystallogr. A* **70**, 636–649 (2014).
39. J. D. Hunter, Matplotlib: A 2D graphics environment. *Comput. Sci. Eng.* **9**, 90–95 (2007).
40. A. P. Thompson, H. M. Aktulga, R. Berger, D. S. Bolintineanu, W. M. Brown, P. S. Crozier, P. J. in't Veld, A. Kohlmeyer, S. G. Moore, T. D. Nguyen, R. Shan, M. J. Stevens, J. Tranchida, C. Trott, S. J. Plimpton, LAMMPS - a flexible simulation tool for particle-based materials modeling at the atomic, meso, and continuum scales. *Comput. Phys. Commun.* **271**, 108171 (2022).
41. W. M. Haynes, Ed., in *CRC Handbook of Chemistry and Physics* (CRC, ed. 97, 2016), pp. 12–16.
42. K. Jin, S. Mu, K. An, W. D. Porter, G. D. Samolyuk, G. M. Stocks, H. Bei, Thermophysical properties of Ni-containing single-phase concentrated solid solution alloys. *Mater. Des.* **117**, 185–192 (2017).
43. A. Singraber, J. Behler, C. Dellago, Library-based *LAMMPS* implementation of high-dimensional neural network potentials. *J. Chem. Theory Comput.* **15**, 1827–1840 (2019).
44. Q.-J. Li, H. Sheng, E. Ma, Strengthening in multi-principal element alloys with local-chemical-order roughened dislocation pathways. *Nat. Commun.* **10**, 3563 (2019).
45. A. G. Khachaturyan, *Theory of Structural Transformations in Solids* (Dover, 2008).
46. G. Kresse, J. Hafner, Ab initiomolecular dynamics for liquid metals. *Phys. Rev. B* **47**, 558–561 (1993).
47. G. Kresse, J. Furthmüller, Efficient iterative schemes forab initiototal-energy calculations using a plane-wave basis set. *Phys. Rev. B* **54**, 11169–11186 (1996).
48. G. Kresse, J. Furthmüller, Efficiency of ab-initio total energy calculations for metals and semiconductors using a plane-wave basis set. *Comput. Mater. Sci.* **6**, 15–50 (1996).
49. M. L. Jenkins, M. A. Kirk, *Characterisation of Radiation Damage by Transmission Electron Microscopy* (CRC, 2000).
50. T. M. Smith, C. A. Kantzos, N. A. Zarkevich, B. J. Harder, M. Heczko, P. R. Gradl, A. C. Thompson, M. J. Mills, T. P. Gabb, J. W. Lawson, A 3D printable alloy designed for extreme environments. *Nature* **617**, 513–518 (2023).
51. B. Schönfeld, L. Reinhard, G. Kostorz, W. Bührer, Short-range order and atomic displacements in Ni–20 at% Cr single crystals. *Phys. Status Solidi B Basic Solid State Phys.* **148**, 457–471 (1988).
52. R. Drautz, Atomic cluster expansion for accurate and transferable interatomic potentials. *Phys. Rev. B* **99**, 014104 (2019).
53. Y. Lysogorskiy, C. van der Oord, A. Bochkarev, S. Menon, M. Rinaldi, T. Hammerschmidt, M. Mrovec, A. Thompson, G. Csányi, C. Ortner, R. Drautz, Performant implementation of the atomic cluster expansion (PACE) and application to copper and silicon. *npj Comput. Mater.* **7**, 97 (2021).

Acknowledgments: We thank C. Ophus for advice on diffraction simulations. **Funding:** This work was supported by the U.S. Department of Energy, Office of Basic Energy Sciences, Materials Sciences and Engineering Division under contract no. DE-AC02-05CH11231 as part of the Damage-Tolerance in Structural Materials (KC13) program. Work at the Molecular Foundry was supported by the Office of Science, Office of Basic Energy Sciences, of the U.S. Department of Energy under Contract No. DE-AC02-05CH11231. Simulations were performed using the Lawrencium computational cluster provided by the IT Division of Lawrence Berkeley National Laboratory (supported by the same office and contract number), as well as award no. BES-ERCAP0021088 of the National Energy Research Scientific Computing Center, a U.S. Department of Energy Office of Science User Facility operated under the same contract number. **Author contributions:** Conceptualization: F.W., M.Z., R.O.R., and A.M.M. Methodology: F.W., M.Z., and A.M.M. Software: F.W. and M.Z. Investigation: F.W. and M.Z. Formal analysis: F.W. and M.Z. Visualization: F.W., M.Z., and R.O.R. Data curation: M.Z. and R.O.R. Validation: M.Z., R.O.R., and A.M.M. Supervision: M.Z., R.O.R., M.A., and A.M.M. Writing—original draft: F.W. and M.Z. Writing—review and editing: F.W., M.Z., M.A., and A.M.M. Project administration: M.Z., R.O.R., and A.M.M. Funding acquisition: R.O.R. and A.M.M. Resources: R.O.R. **Competing interests:** The authors declare they have no competing interests. **Data and materials availability:** All data needed to evaluate the conclusions in the paper are present in the paper and/or the Supplementary Materials. The data for this study have been deposited in Dryad at https://doi.org/10.5061/dryad.qnk98sfr1.

Submitted 10 January 2024
Accepted 27 June 2024
Published 2 August 2024
10.1126/sciadv.adn9673